ARTICLE

Enzyme-Powered Tubular Microrobotic Jets as Bioinspired Micropumps for Active Transmembrane Drug Transport

Liying Wang, Peiting Guo, Dongdong Jin, Yixin Peng, Xiang Sun, Yuduo Chen, Xiaoxia Liu, Wenjun Chen, Wei Wang, Xiaohui Yan, and Xing Ma*

Cite This: *ACS Nano* 2023, 17, 5095–5107

Read Online

ACCESS | Metrics & More | Article Recommendations | SI Supporting Information

ABSTRACT: In nature, there exist a variety of transport proteins on cell membranes capable of actively moving cargos across biological membranes, which plays a vital role in the living activities of cells. Emulating such biological pumps in artificial systems may bring in-depth insights on the principles and functions of cell behaviors. However, it poses great challenges due to difficulty in the sophisticated construction of active channels at the cellular scale. Here, we report the development of bionic micropumps for active transmembrane transportation of molecular cargos across living cells that is realized by enzyme-powered microrobotic jets. By immobilizing urease onto the surface of a silica-based microtube, the prepared microjet is capable of catalyzing the decomposition of urea in surrounding environments and generating microfluidic flow through the inside channel for self-propulsion, which is verified by both numerical simulation and experimental results. Therefore, once naturally endocytosed by the cell, the microjet enables the diffusion and, more importantly, active transportation of molecular substances between the extracellular and intracellular ends with the assistance of generated microflow, thus serving as an artificial biomimetic micropump. Furthermore, by constructing enzymatic micropumps on cancer cell membranes, enhanced delivery of anticancer doxorubicin into cells as well as improved killing efficacy are achieved, which demonstrates the effectiveness of the active transmembrane drug transport strategy in cancer treatment. This work not only extends the applications of micro/nanomachines in biomedical fields but also provides a promising platform for future cell biology research at cellular and subcellular scales.
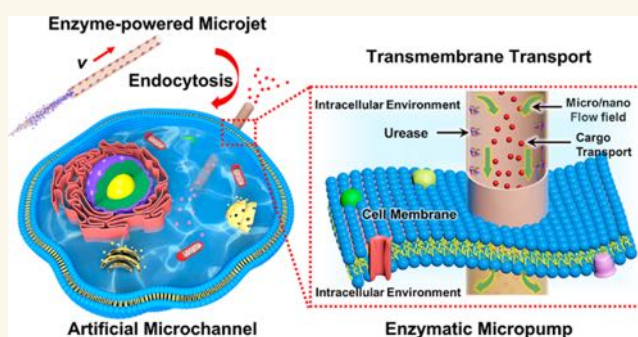
KEYWORDS: silica-based microtubes, enzyme-powered microjets, micropump, transmembrane channel, active drug transport

INTRODUCTION

The cell membrane is a biological semipermeable membrane that isolates the interior area of the cell from the outside environments. It provides a fixed region inside the cell for operating biological reactions, facilitates the cell to interact with other cells, and regulates the transport of substances entering and exiting the cell, all of which are necessary for maintaining cellular activity. Specifically, the exchange of materials between intracellular and extracellular space not only relies on passive diffusion but also, more importantly, can be accomplished against the concentration or electrochemical gradients with the biological pumps located in the cell membrane.[1] This pumping effect, mostly realized by membrane transport proteins, contributes to the supply of ions and nutrients for metabolism and waste discharge out of the cell. Emulating such biological pumps with artificial

systems has long been fascinating to researchers, as it may enable on-demand transmembrane cargo transportation and cellular state detection at the individual cell level with ease, paving the way for better understanding of functions and mechanisms of various cell behaviors.[2] However, the construction of efficient artificial transmembrane channels still remains a grand challenge, due to the stringent requirements on the channel compositions/structures, the interactions with cells, as well as the pumping mechanisms.
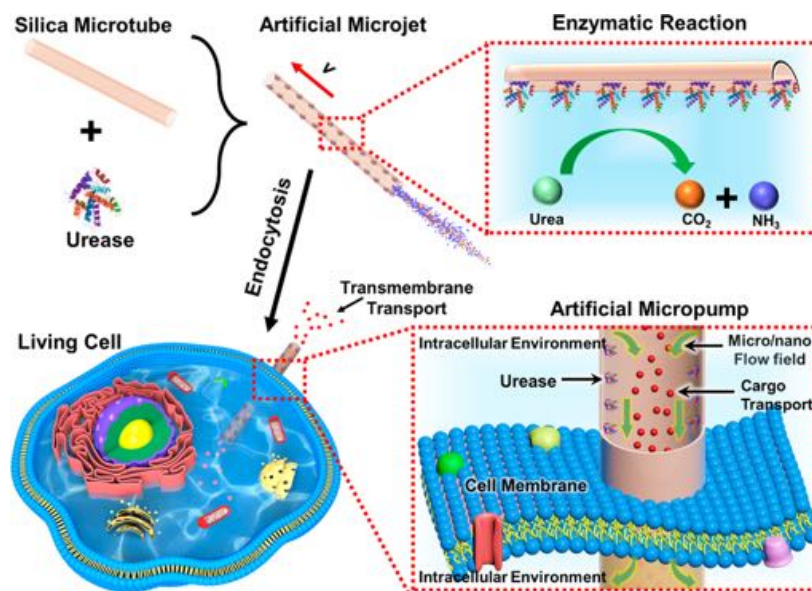
Scheme 1. Schematic Illustration of the Enzyme-Driven Tubular Microjet as a Bioinspired Artificial Micropump for Active Transmembrane Cargo Delivery


To date, several kinds of transmembrane channels have been built by partially "inserting" peptide,[3,4] carbon,[5] silica[6] or supramolecular nanotubes[7,8] into cell membranes. Similar to the biological counterparts, these artificial channels mainly take charge of the substance exchange between the extracellular and intracellular ends, including water molecules,[8,9] protons,[9] ionic species,[10,11] drug molecules,[7] and even genes.[12] For example, by self-assembling cyclic peptides to form a peptide nanotube-based channel in the lipid bilayer, the transport efficiency of molecules with sizes smaller than 1.0 nm (corresponding to the inner diameter of the nanochannel) could be significantly enhanced in a size-selective and dose-dependent manner.[4] Besides, due to the narrow hydrophobic inner pores of carbon nanotubes (CNTs), which resemble the structural motifs typical of biological channels, the insertion of short CNTs into live cell membranes was reported to deliver a variety of species and stochastically sense the change of local channel and membrane charges.[5] However, these nanochannels, either protein pore-based channels or CNT porins, are difficult to be functionalized, and most of them rely on passive diffusion for transmembrane cargo transport, thus lacking an active driving mechanism presented by naturally existing transport proteins.

Micro/nanomachines, which harness and convert energy from external physical fields and/or chemical reactions into mechanical movement, have gained widespread attention and achieved rapid development in the past decade.[13,14] Due to the active and controllable mobility, the functional micro/nano-machines have demonstrated renovating applications in biomedical fields,[15,16] including active targeted drug/gene delivery,[17,18] mini-surgery,[19] cell manipulation,[20] and biosensing.[21] Recently, a few micro/nanomachines have evolved to be an alternative strategy to break through the cell membrane barrier and achieve membrane perforation via exerting mechanical force on the cell surface. For example, ultrasonic field- and light-driven micro/nanomotors could utilize the pulse energy from external fields to instantaneously percolate cell membranes,[18,22−25] while those propelled by magnetic field torque were capable of drilling holes on cell surfaces.[26,27] In this manner, efficient intracellular delivery of the cargos carried by micro/nanomachines (e.g., nucleic acid,[18] caspase-3,[23] oxygen molecules,[24] anticancer drugs,[27] etc.) was achieved for cell treatment or cancerous cell elimination. However, such a strategy generally requires strong and transient forces to punch and/or break cell membranes, which may cause irreversible damage to the cells and often demands high criteria on the manipulation precision of external energy fields. Furthermore, similar to the aforementioned artificial channels, the construction of active transmembrane channels, one of the most distinctive features of biological pumps, still cannot be realized via micro/nanomachines.

In this work, we report the development of bionic micropumps for active transmembrane transportation of molecular cargos across living cells by using enzyme-powered microrobotic jets (Scheme 1). The microjet was prepared by modifying the surface of silica-based microtubes (SMTs) with the urease, which could catalyze the decomposition of urea in the surrounding fluidic environment. In this manner, micro-fluidic flow was produced inside the microtube based on diffusiophoresis and thus generated the thrust force to drive self-propulsion of the microjet along the longitudinal direction. Both numerical simulation and experimental research were conducted to verify the presence of microflow. Then through controllably endocytosing one end of the microjet with a living cell, a transmembrane microchannel was manually established across the cell membrane. With the assistance of microflow, the microrobotic jet transformed into a tubular micropump, which was capable of actively moving cargos between the extracellular and intracellular ends, with immobilized urease serving as a nanoscale engine. Moreover, enhanced delivery of molecular substances (fluorescent propidium iodide and anticancer drug doxorubicin) into living cancer cells was successfully demonstrated by examining the increased fluorescence intensity and killing efficiency of cells, respectively, proving the practical potential of enzyme-powered artificial trans-membrane channels. This work provides a strategy to construct biochemically active micropumps in cell membranes for transmembrane drug delivery, which will inspire more exploration of synthetic micro/nanomachines as biomimetic
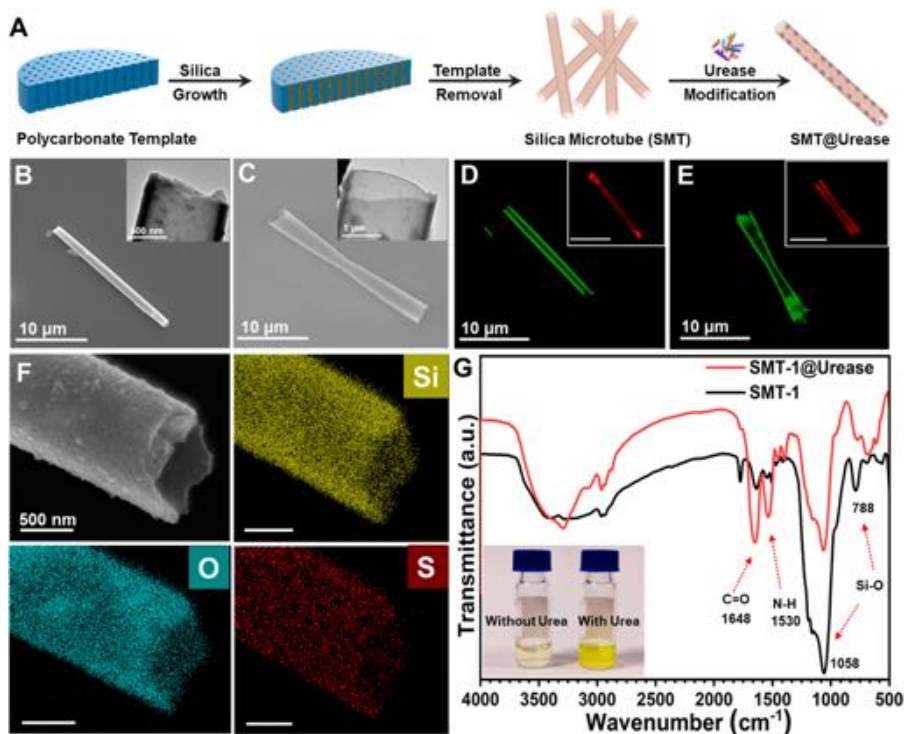
Figure 1. Fabrication and characterization of the SMT and SMT@Urease. (A) Preparation process of SMT and SMT@Urease. (B,C) SEM images of SMT-1 and SMT-2, with the corresponding TEM images shown in the insets. (D,E) CLSM images of the tubular structures of SMT-1 and SMT-2, with the insets showing the distribution of enzyme. (F) EDS analysis of SMT-1@Urease. (G) FT-IR spectra of SMT-1 and SMT-1@Urease, with the colorimetric test in the inset. The concentration of SMT@Urease is 0.1 mg/mL, while urea was added with a concentration of 50 mM. The change of color confirmed the effective biocatalytic performance of the immobilized urease on SMT@Urease.

functional active systems. It will also facilitate future research on cell interfaces, transport in biological channels, and in situ cell condition monitoring at the individual cell level.

RESULTS AND DISCUSSION

Fabrication and Characterization of the Tubular Microjets (SMT@Urease). A template-assisted chemical synthetic strategy is employed to obtain jets with a tubular microstructure, as shown in Figure 1A. A polycarbonate (PC) membrane that possesses uniform holes with an internal diameter of 1 or 2 μm serves as the template. A silica shell was first grown on the internal wall of the holes by sol−gel chemistry.[28] Then the template was dissolved in organic solvent to obtain the dispersed silica-based microtubes (SMTs). Two kinds of microtubes, i.e., SMT-1 and SMT-2 with a diameter of 1 and 2 μm, respectively, were prepared by using the PC templates with different hole diameters. Subsequently, silanization treatment was conducted to endow the surface of SMT with abundant amino groups, which were finally grafted with urease by using glutaraldehyde (GA) as a linker.[29] Scanning electron microscopy (SEM) images in Figure 1B,C and Figure S1 showed the slender morphology of SMT-1 and SMT-2 with a uniform length of ∼20 μm. The inset transmission electron microscopy (TEM) images verified the presence of a hollow structure with a wall thickness of ∼50−80 nm. For the microjets, we modified SMTs and urease with green (fluorescein isothiocyanate, FITC) and red (cyanine 5, Cy5) fluorescent dyes, respectively, followed by confocal laser scanning microscopy (CLSM) observation. As shown in Figure 1D,E, both SMT-1 and SMT-2 demonstrated a through-hole tubular structure without any other materials

blocking the inside channels. Similarly, it could be found from the insets that urease was successfully immobilized and, furthermore, distributed along the whole surface of microjets.

In the energy-dispersive spectroscopy (EDS) results of SMT-1@Urease (Figure 1F), S from the immobilized urease was identified in addition to the major elements of Si and O, proving the presence of urease on the SMT substrate. Besides, in the Fourier transform infrared (FT-IR) spectra, as shown in Figure 1G, the peaks at 1058 and 788 cm^{-1} could be attributed to the stretching vibration of the Si−O−Si bond, indicating the composition of SMT as SiO$_2$.[30] After enzyme modification, the appearance of additional strong absorption peaks at 1648 and 1530 cm^{-1} corresponding to the stretching vibration of carbonyl group (C═O) and bending vibration of amino group (N−H),[31] respectively, further verified that urease was successfully coupled to SMT. Besides, the enzymatic activity of prepared microjets was examined via a colorimetric test. p-Nitrophenol was used as the indicator whose color would change to yellow in the alkaline environment. If the modified urease was active, adding microjets into the solution with a urea substrate and indicator could catalyze the decomposition of urea to ammonia and carbon dioxide, which made the solution become alkaline and thus induced a chromogenic reaction. The inset of Figure 1G well-demonstrated this process, confirming the effective biocatalytic performance of the immobilized urease on the SMT@Urease. We also quantified the loading amount of urease on SMT with a BCA protein assay kit and found that the loading rate is 0.043 mg of urease/mg of SMT (protein loading was calculated based in Figure S2 provided in the Supporting Information).
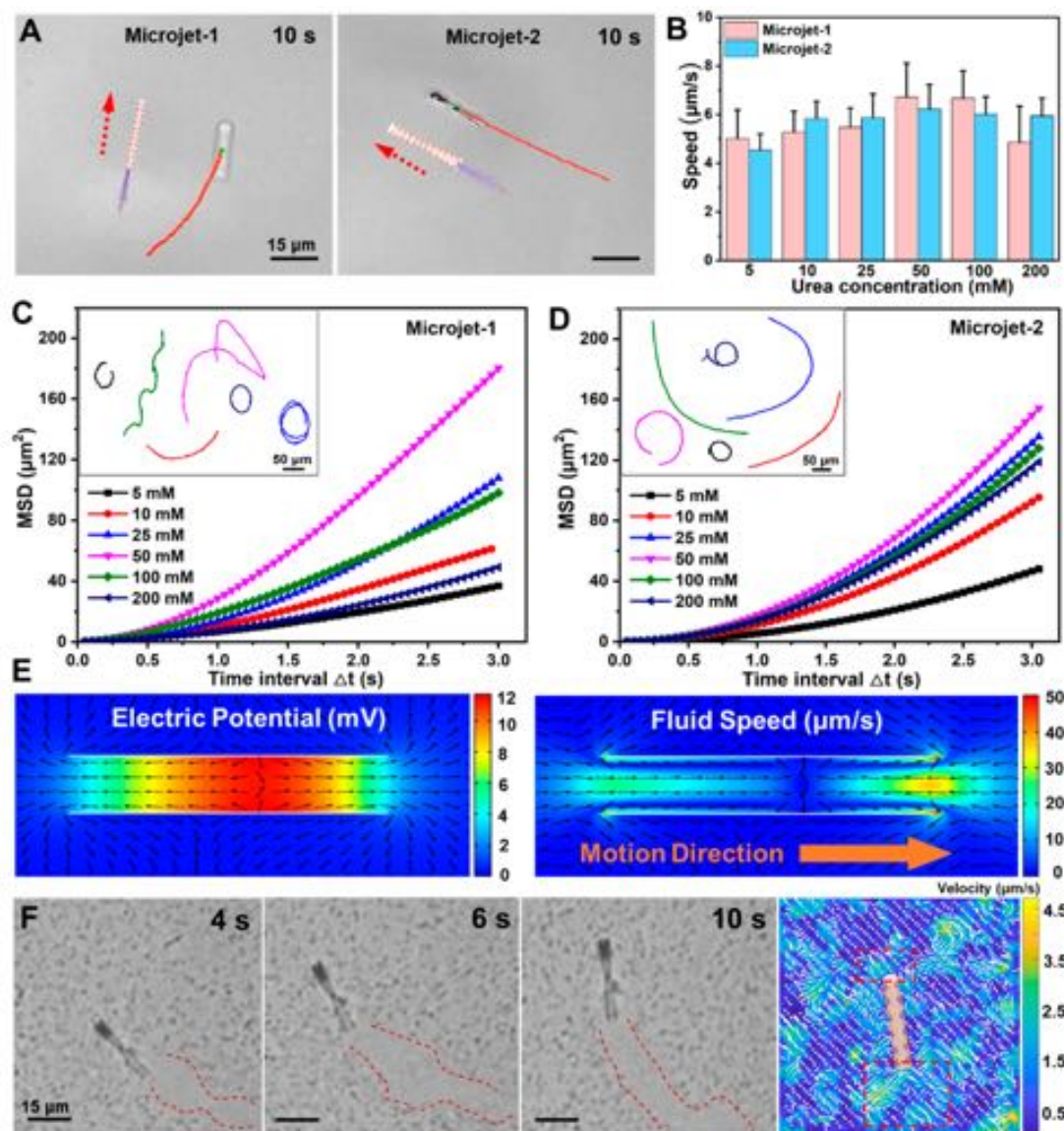
Figure 2. Motion analysis of urease-driven tubular microjets. (A) Screenshots of the motion trajectories of microjets with diameters of 1 and 2 μm (denoted as microjet-1 and microjet-2, respectively). (B) Average velocity of the microjets at different urea concentrations. Error bars indicate standard deviation, $N = 15$. (C,D) MSD analysis of microjet-1 and microjet-2, with the inset showing motion trajectories at different urea concentrations. (E) Simulated electrical potential and flow field distribution of microjet. (F) Time-lapse snapshots of a moving microjet in solution containing tracer silica nanoparticles and the analysis of flow field near its two ends.

Motion Behavior of the Enzyme-Powered Tubular Microjets. After confirming the morphology, distribution of urease, and enzymatic activity of microjets, their motion behavior were investigated. As shown in Figure 2A and Videos S1 and S2, microjets with diameters of 1 and 2 μm exhibited active self-propulsion along their longitudinal direction in urea solution with the driving force from the enzyme-catalyzed reaction. Then the average velocity of microjets was calculated based on their translational motion trajectories, which depended on the concentration of urea (Figure 2B). In our study, when urea concentration was increased from 5 to 200 mM, the speed of both microjets first reached a maximum value (e.g., ~6.47 μm/s for microjet-1 at 50 mM, which is ~1.35 times that at 5 mM) and then decreased slightly. This was because the enzymatic reaction rate did not increase monotonously with the increase of the substrate concentration. There was an optimal concentration for the enzyme-catalyzed

reaction, beyond which enzymatic activity would be inhibited, inducing the slowdown of movement. In comparison to the previous reports of urease-driven micro/nanomotors,[29] the fuel-dependent motion behavior of the microjets is less apparent in this study. Meanwhile, it could be found that the size had little effect on motion speed for the urease-powered microjets, which may be explained by the random distribution of urease on the tubular structure at a small scale and the difference in the amount of urease modified on the tubes.[32] Further mean square displacement (MSD) analysis results of microjet-1 and microjet-2 are shown in Figure 2C.D, respectively, in which all of the curves exhibited a distinct parabolic shape, thus indicating the long-range and directional motion behavior of microjets. Typical tracking trajectories in different urea concentrations are also displayed in the insets. The directional motion was mainly ascribed to the urease anchoring on the inner wall of tubular jets, while those outside
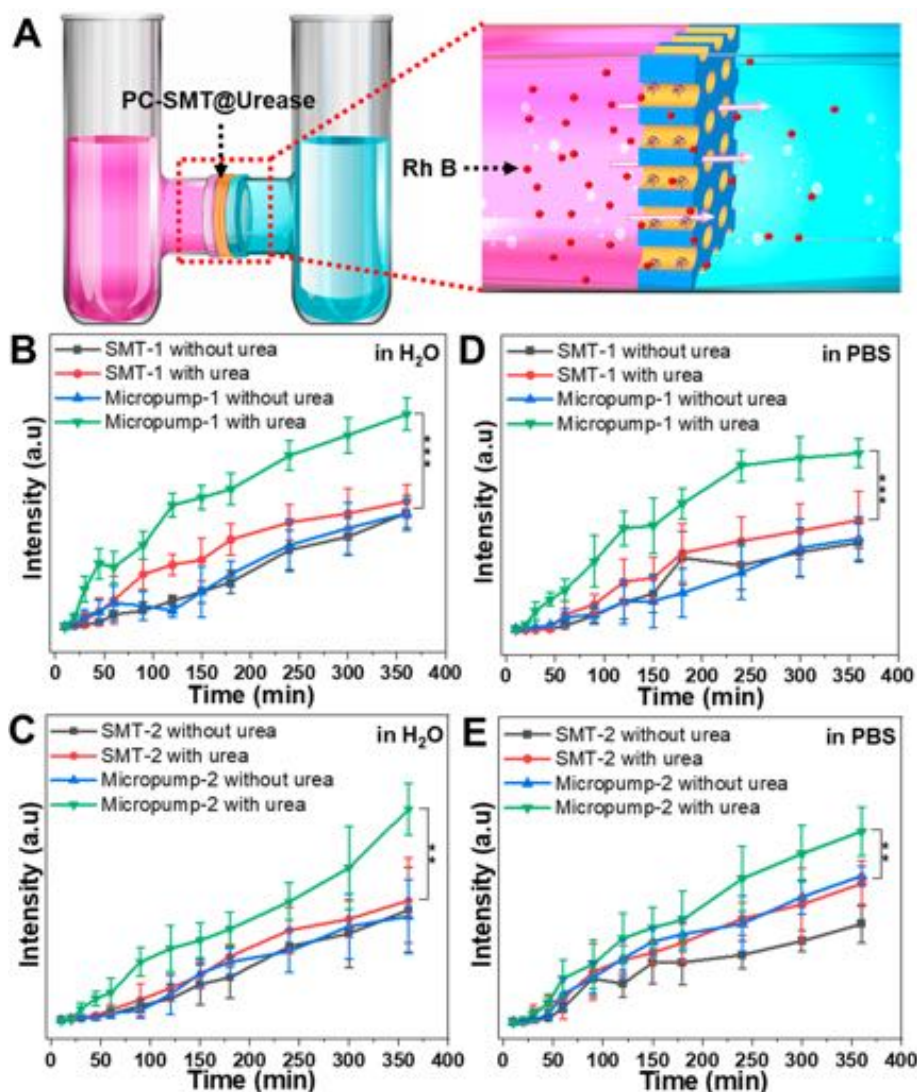
Figure 3. Enhanced transportation of molecular substances passing through the microchannels using urease-powered microjets as micropumps. (A) Schematic diagram of the experimental setup of the enzyme-powered micropumps. (B,C) Change of fluorescence intensity of the solution in the right container of the setup with micropump-1 and micropump-2 in DI H_2O. (D,E) Change of fluorescence intensity of the solution in the external container with micropump-1 and micropump-2 in PBS. The urea concentration is 50 mM. Error bars indicate standard deviation, $N = 4$. P values are calculated using the t test, **$P < 0.01$, ***$P < 0.001$.

the tube mainly contributed to the rotational motion, which was explained in our previous work.[33]

Numerical simulation was performed to obtain an in-depth understanding of the self-propulsion mechanism of the urease-driven tubular microjets. The propulsion force of urease-driven motors came from the biocatalytic decomposition of urea which produced NH_4^+ and OH^- ions in solution. Due to the different diffusion rate of these two positive and negative ions, an outward electric field and a corresponding fluid field were spontaneously established outside the electric double layer of the micro/nanomotors to maintain electrical neutrality and, more importantly, to propel the motors.[29] Based on the expected mechanism of ionic diffusion electrophoresis, in this model, we assumed that the inner wall of the tubes had urease catalytic activity which was the main contribution of longitudinal movement. The effect of enzymatic reaction product CO_2 and related ions was neglected as they are much less soluble compared to NH_3. Because of the inherent nonhomogenous distribution of urease on the inner wall of

microjets,[32] the two ends were prone to be subjected to different electric field forces, resulting in a directional motion. Figure 2E shows the simulation results of the electric field and fluid field distribution of the tubular microjets. The direction of the electric field inside the tube pointed from the inside to the outside because the diffusion of OH^- (5.27×10^{-9} m^2/s) was much faster than that of NH_4^+ (1.95×10^{-9} m^2/s), while the corresponding fluid field exhibited an opposite distribution direction. SiO_2 tracer nanoparticles with an average diameter of ~650 nm were added to visualize the ionic diffusion-induced electric field and the existence of surrounding flow field around the microjets. Typically, the tracer nanoparticles near the tail of microjets were significantly repelled away as the translational motion of the tubular motor advanced, which are found in Figure 2F and Video S3. By analyzing the flow field via particle image velocimetry, a relatively obvious fluid field at the tail of the tubular microjet was visualized. The repelling regions of the tracer nanoparticles at the head or tail of the microjets had different sizes (Figure S3 and Video S4), which

might illustrate that nonuniform fluid forces existed on these two ends and thus caused the directional motion. Such a repelling effect should be attributed to the electric force exerted by the self-built electric field around microjets or the density gradient-induced flow field generated by the enzyme-catalyzed reaction inside the tube.[34] Besides, it is worth noting that tracer nanoparticles close to the head of the moving microjets might be even "pulled" into the opening "mouth" of the hollow tubular jets and then expelled from the other end (Figure S4 and Video S5), which indicated the continuous flowing fluid inside the channels of biocatalytically active tubular microjets.

Most of the reported chemically powered tubular micromotors are driven by the formation of gas bubbles through the catalytic reactions triggered by chemically active components or catalysts immobilized on the inner wall of tubes, such as Zn,[35] Pt,[36] and catalase.[37] In our previous work, we reported the bubble-free propulsion of ultrasmall tubular nanojets with a diameter of only 220 nm.[33] The tubular microjets in this work were much larger in size (the diameter was 1 or 2 μm, and the length was ∼20 μm), proving that the mechanical energy converted from the urease-catalyzed biochemical reaction is sufficient enough to propel microscale tubular jets without generating bubbles. On the basis of the above findings, it can be concluded that, when fueled with urea, the enzymatic reaction inside the microjets would produce a self-propulsion force via an ionic diffusiophoresis mechanism based on the asymmetry of enzymatic activities. Characterizing the motion behavior can also prove the driving force caused by the urease catalysis to the microjet, and then the moving microjet will cause the microfluid motion around it. When the microjet is fixed, the surrounding fluid field still exists, and the urease-catalyzed reaction in the tube can still induce the microflow, which is equivalent to playing the role of a micropump. Therefore, apparent microfluidic flow inside the hollow cavity of the microjets would be generated in the enzymatic tubular jets, which might be favorable for molecular cargo transportation passing through the microtubes by the potential pumping effect.

Enzymatic Reaction-Enhanced Cargo Transport through the Microjets. Previous reports indicated that the concentration gradient generated by enzymatic reactions would induce a directional flow of the surrounding fluid to serve as catalytic pumps.[34,38−43] Encouraged by the observed flow field within the tubular microjets, we used an experimental setup reported by Hess et al.[44] to simulate the function of transmembrane cargo transportation by transforming microjets into artificial micropumps. Right after the growth of the silica shell, we directly immobilized enzymes onto the internal walls of the microtubes instead of extracting them from the PC template, thus obtaining a PC film with numerous urease-modified microchannels connecting the two sides of film, denoted as PC-SMT@Urease. Figure 3A shows the schematic diagram of the setup, where the PC-SMT@Urease, an analogous of the cell membrane, served as a physical barrier separating the solution at two sides. The enzyme-functionalized tubular micropumps were inherently embedded inside the PC membrane, mimicking the biological pumps on the living cell membrane. A solution containing 5 μg/mL Rhodamine B (Rh B, model cargo molecules) was initially added to the glass bottle on the left (left side of the PC membrane), while pure water or phosphate-buffered saline (PBS) solution was added into the right container (the other

side of PC membrane). The diffusivity of Rh B passing through the microchannels was monitored by measuring the fluorescence intensity of Rh B in the right container solution. Figure 3B,C shows the time-dependent changes of the fluorescence intensity when using PC-SMT@Urease with hole diameters of 1 and 2 μm (micropump-1 and micropump-2) in deionized (DI) H$_2$O, respectively. It was found that the fluorescence intensity of the micropump with urease modification and the presence of urea (green line) was always higher than that of the control group (SMT without urea, SMT with urea, and micropump without urea), which implied that Rh B diffused more rapidly across the microchannels from the left side of the solution to the right when the enzyme-catalyzed reaction took place. Moreover, we obtained P values (**P < 0.01, ***P < 0.001) through the t test, which also indicated that the experimental group was significantly different from the control group, and the urea substrate could activate the micropump to enhance the Rh B diffusion transport.

Considering the influence of ionic strength in real physiological environment, the experiments were repeated in PBS (pH 7.4), and similar results were found, as shown in Figure 3D,E, suggesting that the tubular micropumps could work in future biological conditions. Such efficient pumping in PBS buffer also proved that the pumping mechanism could be attributed to the catalytic reaction-induced density gradient rather than electrophoresis.[34,38,40,43,45] Moreover, to exclude the influence of urea substrate addition on the density gradient, we fabricated the group of transmembrane microchannels without modification of urease. When urea was added, the diffusion rate of Rh B passing through the channels to the right solution was not obvious in this group. The finding not only excluded the influence of urea fuel on the pumping effect but also certified the biocatalytic reaction-powered pumping mechanism. The above proof confirmed that our envisioned enzyme-driven microjets could serve as a micropump to actively enhance the diffusion and transport of substances across the membrane barriers with the assistance of microflow.

Establishment of Artificial Transmembrane Microchannels on Living Cell Membrane. In almost all of the previous studies of micro/nanomotor-based intracellular cargo delivery systems, transient mechanical force was directly used to "open" the cell membrane. In this work, as shown in Scheme 1, we proposed to construct the artificial transmembrane micropump with a gentle approach, i.e., natural endocytosis of tubular microjets by cells. The feasibility of establishing transmembrane microchannels with pure microtubes was first confirmed in this section. The biocompatibility of the silica tubes was evaluated by a cellular cytotoxicity experiment, as shown in Figure S5, which showed negligible cytotoxicity toward HeLa cells. We previously demonstrated endocytosis-enabled construction of transmembrane channels by using nanosized silica tubes.[6] Hereby, microsized silica tubes were cocultured with living HeLa cells to build the artificial transmembrane channels through endocytosis. It was found that the cells could hardly internalize SMT-2, probably due to the larger size of tubes. In contrast, SMT-1 could be effectively internalized by the living cells and thus used in our subsequent experiments (denoted as SMT for convenience). The CLSM images in Figure S6A showed that with the increase of coculture time, one end of SMT was gradually endocytosed by the cell. SMT and cells were cocultured for about 4 h, and SMT could be partially endocytosed by cells, thereby establishing the transmembrane microchannels. Figure S6B is
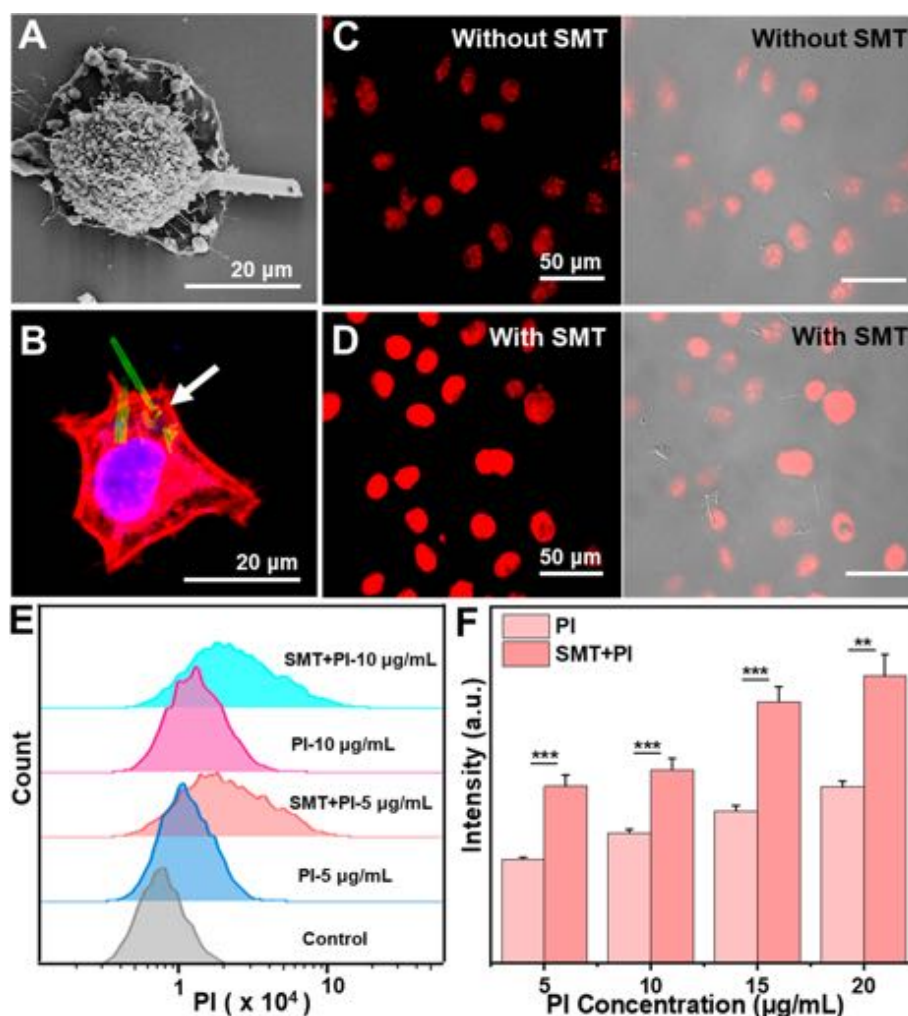
Figure 4. Establishment of artificial transmembrane microchannels through the endocytosis of SMT into living HeLa cells. (A,B) Cryo-SEM image and CLSM image of a SMT-1 half endocytosed by a cell. SMT and HeLa cells were cocultured for 4 h. (C,D) Red fluorescent and red fluorescent/bright-field merged CLSM images of the HeLa cells without/with addition of SMT. After SMT and cells were cocultured for 4 h, adding PI (5 μg/mL) and continuing to incubate for 20 min. (E) Histogram of PI fluorescence intensity in HeLa cells with/without SMT under varied PI concentrations of 0, 5, and 10 μg/mL, obtained by flow cytometry analysis. (F) Statistic summary of PI fluorescence intensity in HeLa cells with and without SMT. Error bars indicate standard deviation, $N = 3$. P values are calculated using the t test, **$P <$ 0.01, ***$P <$ 0.001.

the bright-field images of SMT and HeLa cells cocultured for 4 h, showing that the SMT was endocytosed as a transmembrane channel. Figure 4A,B exhibits the typical cryo-SEM image and CLSM image of a SMT entering into a cell after 4 h, respectively, clearly demonstrating that one end of the SMT was "penetrating" inside the cell and the other end left outside. It could be found that the tubular structure of the SMT labeled with green fluorescence is embedded inside the cytoskeleton labeled with red fluorescence. Figure S7 shows typical CLSM images of the interaction between SMT@FITC and HeLa cells, and Video S6 shows the corresponding video of the reconstructed 3D CLSM imaging. Although complete endocytosis of SMTs was also observed, most of them were partially endocytosed by the cells, establishing the artificial transmembrane microchannels. We used the red membrane dye (DiI) to stain the cell membrane of the HeLa cells after the microchannels were established to investigate the integrity of the cell membrane after the endocytosis of SMT@FITC. From the cross section of the CLSM images (Figure S8), it shows that the green SMT@FITC is embedded in the red cell

membrane, and the cell membrane can maintain a normal and complete shape. Besides, time-dependent CLSM observation on the interaction between SMT and living HeLa cells was carried out (Figure S9), showing that most of SMT@FITC could be endocytosed by the cells when the coculture time was 4 h. Therefore, this coculture period was applied in the subsequent experiments.

In order to investigate the potential of using the established microchannels for transmembrane cargo delivery, propidium iodide (PI) was chosen as a model drug or indicator because of its selective permeability toward cell membranes. Figure 4C,D shows the CLSM images of cells stained with PI at a concentration of 5 μg/mL. The microchannel was established after the SMTs were cocultured with HeLa cells for 4 h and then coincubated with PI for 20 min. In the presence of SMT, the fluorescence intensity of PI entering into the cells was relatively stronger than that without SMT. Flow cytometry experiments were performed to quantify the fluorescence intensity of PI entering the cells with or without SMT (Figure 4E,F). A corresponding scatter diagram of flow cytometry
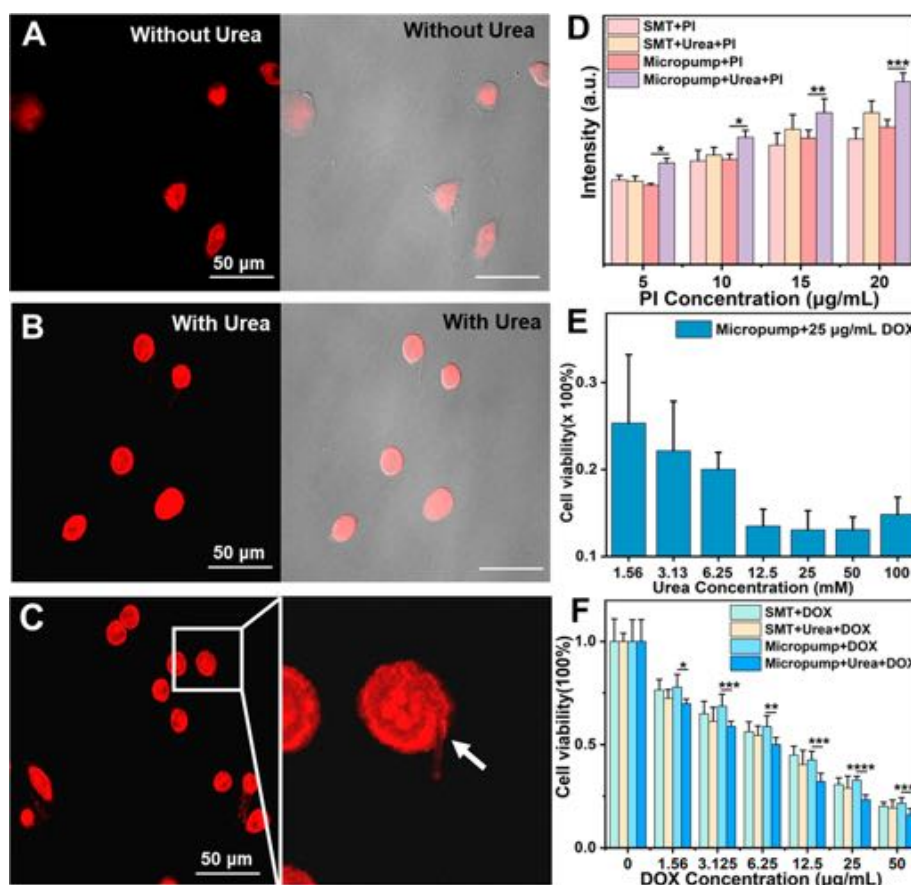
Figure 5. Active intracellular drug delivery and anticancer efficacy by the urease-driven micropumps. (A,B) Red fluorescent and bright-field merged CLSM images of the HeLa cells cultured with PI and microjets in the absence and presence of urea fuel, respectively. The incubation time of HeLa cells with PI (5 μg/mL) was 20 min. (C) Enlarged CLSM image showing the micropump-1 inserted into the cytoplasm of a single cell. (D) Flow cytometry analysis of the fluorescence intensity of HeLa cells cultured with varied concentrations of PI. Error bars indicate standard deviation, $N = 3$. P values are calculated using the t test, *$P < 0.05$, **$P < 0.01$, ***$P < 0.001$. (E) Viability of HeLa cells with micropump at a DOX concentration of 25 μg/mL under different urea concentrations. The incubation time of HeLa cells with DOX was 20 h. Error bars indicate standard deviation, $N = 6$. (F) Viability of HeLa cells with micropump under different DOX concentrations. The incubation time of HeLa cells with DOX was 20 h. Error bars indicate standard deviation, $N = 6$. P values are calculated using the t test, *$P < 0.05$, **$P < 0.01$, ***$P < 0.001$, ****$P < 0.0001$.

assay is given in Figure S10, where the cells in the rectangle range were selected for statistics to ensure counting on intact cells and thus data accuracy. Typical histograms of the PI fluorescence intensity all right-shifted with the addition SMT for PI concentration of both 5 and 10 μg/mL. For different PI concentrations, all of the groups with SMT showed significantly increased fluorescence intensity, further proving that SMT could assist PI molecules to enter into the cells via passive diffusion through the inner microchannels. Furthermore, we used hydrogel (gelatin) to fill the hollow structure of SMTs to obtain the SMT@Gel (Figure S11 shows the SMT@ Gel with nonhollow structure). By comparing SMT and SMT@Gel, as shown in Figure S12A, SMT@Gel has a weaker ability to deliver PI than SMT. The reason is that the gelatin filled in the hollow structure would hinder the PI molecule transport into the HeLa cells. As shown in Figure S12B, the SMT@Gel also showed a similar performance on DOX transport. It also confirmed that the drugs can enter cells through microchannels established on the cell membrane. These results demonstrated that the spontaneous endocytosis of SMT by the living cells could successfully establish artificial transmembrane microchannels, which laid the foundation for the following study on transmembrane active micropumps.

Active Transmembrane Drug Delivery Enabled by Enzyme-Powered Tubular Micropumps. After certifying the enhancement of transporting efficiency via the enzymatic reaction inside microjets and the feasibility to establish transmembrane artificial microchannels, construction of enzyme-driven micropumps across the cell membrane through the endocytosis of microjets was further investigated. CLSM images in Figure 5A,B show the red fluorescence color of PI molecules entering into the cells after cocultured with microjet-1 with and without urea substrate, respectively. When urea was not available, PI could either enter the cells through the microchannels inside microjets or directly diffuse through the cell membrane, leading to a certain degree of red fluorescence intensity. However, with the addition of urea fuel, the fluorescence intensity of PI in the cells was enhanced, suggesting the effective function of the enzyme-driven tubular microjets as micropumps that could actively promote the delivery of PI molecules across the cell membrane. Figure 5C shows an enlarged CLSM image of a single cell where the arrow is pointing to a micropump penetrating into the cell. There was also a red fluorescence color inside the microtube, indicating that the PI molecules indeed passed through the microchannel of the micropump to enter the cell. The effect of

enhanced transmembrane cargo transport by the micropump was also quantified by flow cytometry analysis. The results, as shown in Figure 5D, indicated that, under different PI concentrations, the fluorescence intensity of the experimental group (micropump with urea) with urease catalytic activity would be higher than that of the control group (SMT without urea, SMT with urea, and micropump without urea). It is suggested that the action of enzyme-powered micropump would drive more PI molecules to enter the cells and improve the efficiency of intracellular cargo delivery across the cell membrane barrier.

The anticancer drug doxorubicin, DOX, was used to evaluate the enhanced intracellular drug delivery efficacy of the enzymatic micropumps. The cytotoxicity of urea was first tested to exclude the influence of the fuel (Figure S13). The MTT assay results indicated that urea had low toxicity, and the viability of cells with or without adding SMT remained above 80% even under 100 mM urea concentration. Then we further evaluated the cancer killing effect of the delivered DOX by the enzymatic micropumps. As shown in Figure 5E, the concentration of DOX was kept at 25 μg/mL, with the increase of urea concentration, the viability of the cancer cells decreased significantly. When the concentration of urea was higher than 12.5 mM, the viability of HeLa cells was only about 15%. The results revealed a positive correlation between the cancer killing effect and urea fuel concentration, which implied that the increased enzymatic activity could promote more drug molecules to enter the cells by the pumping mechanism. Furthermore, as shown in Figure 5F, micropumps were established on these groups of cells with and without urea, respectively, under varied concentrations of DOX, and the SMTs with and without urea were compared as the control groups. The cell viability of these groups decreased with increasing DOX concentration. At the same concentration of DOX, the cell viability of the group with catalytic activity (the micropump with addition of urea fuel) was always lower than those of control groups (SMT without urea, SMT with urea, and micropump without urea) without urease catalytic activity. We believe that density-driven fluid flow should be at least one possible mechanism for the enhanced drug delivery by the enzymatic micropumps. It is speculated that the concentration gradient of reactants and/or products along the microchannels would be formed when the enzyme catalyzed the decomposition of the substrate urea, which further promoted the flow diffusion within the microchannels and therefore facilitated the entry of extracellular substances into the cells. Nevertheless, our experimental results fully confirmed the active transmembrane drug delivery by the enzyme-driven micropumps.

CONCLUSION

In summary, we demonstrated the application of a self-propelled enzymatic tubular microjet as a bioinspired artificial micropump to enhance the transmembrane drug delivery toward living cancer cells. First, silica-based enzymatic microjets with well-defined geometry (diameter: 1 and 2 μm, length: 20 μm) were fabricated, which exhibited chemical-fueled directional self-propulsion. Numerical simulation and experimental observation with tracer nanoparticles revealed that the motion of the microjets was driven by ionic diffusiophoresis mechanism. Encouraged by the enzymatic reaction-induced microfluidic flow inside the microtubular structure, we explored the potential of using these microjets as artificial micropumps for transmembrane delivery. Through natural endocytosis of microjets into living HeLa cells, artificial transmembrane active microchannels were successfully established to mimic the biological pumps naturally located on cell membrane. Such "embedded" artificial microchannels successfully facilitated the entry of PI molecules into the cells and could further enhance the intracellular drug delivery efficiency when functioned as enzyme-driven micropumps.

Though we successfully demonstrate the attempt of using enzyme-powered microjets as artificial micropumps for active transmembrane cargo transport, the current system can be further improved in future investigations. For instance, control on the pumping direction is absent in the current system, which will for sure significantly improve the intracellular transportation efficacy or even realize extraction of intracellular substances. Furthermore, in-depth exploration on the microfluidic field inside the tubular structure by direct visualization will definitely reveal more fundamental knowledge about the pumping mechanism, though great technique challenges faced. Besides, future study on transmembrane delivery of large biological molecules (e.g., nucleic acids or proteins) and in situ monitoring of cells would bring more practical significance to the current system. In summary, this study demonstrates a bioinspired micro/nanopump-enabled transmembrane cargo transportation, which is of great interest for future exploration of biomedical applications of synthetic micro/nanomachines.

MATERIALS AND METHODS

Materials and Characterization. Materials included polycarbonate (PC) filtering membrane with diameters of 1 and 2 μm (catalog no. 7060-4710 and no. 7060-2511, Whatman, Maidstone, UK), tetraethylorthosilicate (TEOS), 3-aminopropyltriethoxysilane (APTES), triethanolamine (TEOA), urease (U4002-20KU, purchased from Sigma), glutaraldehyde (GA, 50% in H_2O), alumina polishing powder (the particle size is about 2.5 μm), urea (CH_4N_2O), p-nitrophenol ($C_6H_5NO_3$), Rhodamine B (Rh B), anhydrous ethanol (EtOH), N,N-dimethylformamide (DMF), sodium hydroxide (NaOH, 100 mM), fluorescein isothiocyanate (FITC), 1,1′-dioctadecyl-3,3,3′,3′-tetramethylindocarbocyanine perchlorate (DiI), gelatin (strength ~250 g Bloom), cyanine 5 (Cy5), Dulbecco's modified Eagle's medium (DMEM), fetal bovine serum (FBS), trypsin-EDTA, antibiotics, Triton X-100, albumin from bovine serum (BSA), phosphate buffered saline (PBS), 3-(4,5-dimethyl-2-thiazolyl)-2,5-diphenyl-2H-tetrazolium bromide (MTT), dimethyl sulfoxide (DMSO), polyoxymethylene (($CH_2O)_n$), phalloidin-tetramethylrhodamine B isothiocyanate (phalloidin-TRITC), 4′,6-diamidino-2-phenylindole (DAPI), and HeLa cells. Scanning electron microscopy (SEM) images and energy-dispersive X-ray (EDX) spectroscopy were captured with a Carl Zeiss GmbH Gemini SEM 300 microscope and Oxford instruments X-Max, respectively. Optical videos were taken by a Leica inverted optical microscope (Leica DMi8) with a 40× air objective. CLSM images were taken by confocal laser scanning microscope (NiKon A1). The fluorescence intensity of Rh B was obtained with a Thermo RF 5301 instrument. The absorbance of HeLa cells was measured by microplate reader (Infinite F50, Tecan). The fluorescence intensity of cell samples was characterized by flow cytometry (Cyto FLEX, Beckman Coulter).

Fabrication of Silica Microtubes and Enzyme-Driven Tubular Microjets (SMT@Urease). The SMTs with pore sizes of 1 μm (SMT-1) and 2 μm (SMT-2) were synthesized using a PC membrane as the template.[28] SMT-1 was prepared as follows: TEOA (60 mg) was dissolved in 24 mL of water in a glass vial where the polycarbonate membrane with a pore size of 1 μm was placed. The mixture was heated to 80 °C, and 30 μL of APTES was added under stirring. After 30 min at a constant temperature, 280 μL of TEOS was added and the reaction was kept at 80 °C for 4 more hours. The preparation for SMT-2 was similar to the process described above: TEOA (10 mg) was dissolved in 6 mL of water in a glass vial where

the PC membrane with a pore size of 2 μm was placed. The mixture was heated to 80 °C, and 7.5 μL of APTES was added under stirring. After 30 min at a constant temperature, 45 μL of TEOS was added and the reaction was kept at 80 °C for 2 more hours. After the reaction, the surface of the PC membrane was rinsed with ethanol and polished on both sides using a wet cotton swab dipped in alumina powder to remove silica from the surface. Finally, the PC membrane template was dissolved in DMF for 30 min, and the free SMT was washed in DMF, EtOH, and DI water 2 times sequentially. Then SMTs were dispersed in DI water for further use. Afterward, the urease was modified on the inner and outer walls of the silica tubes using glutaraldehyde as a linker to prepare the tubular silica microjets (SMT@Urease). The specific step is to disperse the free SMTs obtained in the previous step in DI water (1 mL) containing glutaraldehyde (50 μL). The mixture solution was kept shaking for 3 h, and then the GA-activated SMTs were washed with DI water five times and resuspended in PBS (1 mL) containing urease (5 mg). The mixture was shaken at room temperature for 16 h. The SMT@Urease was obtained after washing with DI water five times. Finally, the products were suspended in DI water and stored at 4 °C for further use. Figure 1A describes the detailed fabrication of the enzyme-driven tubular microjets (SMT@Urease).

Fabrication of Gelatin-Filled Silica Microtubes (SMT@Gel). Silica microtubes were pregrown in the pores of the PC membrane according to the above process, and 10% gelatin solution was filled into the pores of the PC membrane by vacuum filtration and finally placed in a 4 °C refrigerator to solidify the gelatin solution.

Characterization of Enzyme Activity. The catalytic activity of urease was assayed using the property that p-nitrophenol develops color in alkaline solutions, as well as validating the successful modification of urease in SMTs. 100 μL of p-nitrophenol solution (0.08 wt %) and 100 μL of urea solution (100 mM) were mixed well in a glass vial. Then 100 μL of DI water was added to the control group and 100 μL SMT@Urease to the experimental group. These were mixed well and left to stand for 10 min, and the color change of the solution in the bottle was then observed when the reaction was complete.

Motion Observation of the Enzyme-Driven Tubular Microjets (SMT@Urease). The optical video was recorded by using a Leica DMi8 with a 40× objective lens to study the movement of the tubular microjets. The aqueous solution of SMT@Urease (10 μL) with proper concentration and urea solution (10 μL) with varying concentrations (5, 10, 25, 50, 100, 200 mM) were placed in a 0.8 mm high Petri dish. With the same strategy, the movement behavior of tubular microjets in the silica nanoparticle (as tracer particles) suspension containing 25 mM urea was observed. The videos of the movement condition of motors were recorded via a CCD camera at the frame rate of about 20 fps.

COMSOL Simulation. The equations and boundary conditions of our numerical model are described as below. This model was originally developed by Velegol et al.[46] and was recently adapted by Wang et al.[47] for the study of PMMA/AgCl self-diffusiophoretic micromotors. We assume that the reactions and flows are at steady-state and independent of time. Also, we employ the infinitesimal electric double layer (EDL) approximation. The active surface of the particles in our model produces ions (NH_4^+ and OH^-) at a constant flux J. The electrical boundary condition at the double layer of the active surface is then set by the normal potential gradients:

$$-(\partial\varphi/\partial n) = Jk_BT/(2en_0(1/D_+ - 1/D_-)) \tag{1}$$

where φ is the electrical potential, k_B is the Boltzmann constant, T is the absolute temperature, e is the elementary charge, n_0 is the bulk concentration of ions, and D_+ and D_- are the diffusion coefficients of NH_4^+ and OH^-, respectively.

The surface electrical boundary condition for the inert surface is $-(\partial\varphi/\partial n) = 0$ because of no flux. Outside the electrical double layer, the electrostatic problem is defined by the Laplace equation ($\nabla^2\varphi = 0$). The electrohydrodynamic problem is governed by the Stokes equations:

$$\eta\nabla^2\boldsymbol{u} = 0 \tag{2}$$

$$\nabla\cdot\boldsymbol{u} = 0 \tag{3}$$

where η is the dynamic viscosity of the solution and $\boldsymbol{u}$ is the flow fluid velocity. The boundaries of the micromotor are set to be electro-osmotic, with a slip velocity:

$$U = \zeta p\varepsilon E'/\eta \tag{4}$$

where ζp is the zeta-potential of the micromotor, ε is the medium permittivity, and E' is the tangential component of the local electric field.

This numerical model was solved by a finite-element package (COMSOL Multiphysics 5.4, Burlington, MA, USA). The default parameters in the simulations are set as the following values: J of the two ends of the tube are 10^{-7} mol/(m^2·s) and 3×10^{-7} mol/(m^2·s), $\zeta p = -20$ mV, $D_+ = 1.95 \times 10^{-9}$ m^2/s, and $D_- = 5.27 \times 10^{-9}$ m^2/s. The tubes are placed in a water-filled simulation block of 40 μm in length, 40 μm in height, and 40 μm in width. The size of the tube is 2 μm in inner diameter and 20 μm in length.

Diffusion Model of Substance Enhanced by Enzyme-Driven Tubular Micropumps (SMT@Urease). The model consists of two cylindrical glass bottles with interconnected structures, so that the left and right sides form the feed compartment and the receptor compartment. The composition structure is similar to the H-type electrolytic cell, and the PC membrane is equivalent to the proton membrane. As shown in Figure 3A, a layer of silica was preformed in the pores of the PC membrane and urease were modified on the inner wall of the tube. The PC-SMT@Urease served as the diffusion transport channel for the left and right compartments. We made the left as the feed compartment and the right as the receptor compartment. The receptor compartment is an aqueous solution or PBS solution containing 50 mM urea, while the feed compartment is Rh B solution (5 μg/mL). Trace amounts of the solution (50 μL) were removed from the receptor compartment at different time points, and the diffusivity of Rh B was compared by measuring the fluorescence spectra of the solution from the receptor compartment (the fluorescence intensity was obtained by Thermo RF 5301, $E_x = 540$ nm, $E_m = 578$ nm).

Cell Experiment and Characterization. In this work, we mainly used cervical cancer cells (HeLa) for in vitro cell experiments, including cytotoxicity test, confocal laser microscopy characterization, and flow cytometry.

Cytotoxicity Test (MTT Assay). The absorbance of HeLa cells was measured with a microplate reader (Infinite F50, Tecan), and the toxicity of HeLa cells to different samples and different experimental conditions was characterized. HeLa cells were seeded into a 96-well plate at a density of 5×10^3 cells per well in 100 μL of medium and cultured in 5% CO$_2$ at 37 °C for 12 h. Ten microliters of different concentrations of sample solutions was added to each well and cocultured with cells continuously for 20 h. After this, the cell medium was removed and 100 μL of MTT solution (0.5 mg/mL) was added to each well and left to incubate for another 4 h. Subsequently, the liquid was aspirated from the 96-well plate, and 100 μL of DMSO was added to each well. Finally, the absorbance of each well was measured at a wavelength of 570 and 490 nm using a microplate reader. Cell activity was calculated using the following formula: cell viability (%) = (mean of absorbance value of treatment group/mean of absorbance value of control) × 100%. Six replicates were conducted for statistical analysis ($N = 6$). The effects of SMT and urea on cytotoxicity were investigated in this study. In addition, MTT assays were also used to verify the role of artificial transmembrane channels (SMT, SMT@Urease) on DOX transmembrane delivery. The procedure was the same as above. After the HeLa cells were adhered to the 96-well plate, 10 μL of SMT suspension or SMT@Urease suspension was added and the sample was cocultured with the cells for 4 h to allow the cells to endocytose at one end of the micron tube. To the wells in the 96-well plates was then added DOX solution at different concentrations.

CLSM Observation and Cell Staining. The human cervical cancer cells (HeLa cell) were cultured with DMEM containing 10% FBS and 1% antibiotics at 37 °C in a 5% CO_2 atmosphere. The nucleus and cytoskeleton of the HeLa cells were stained in experiments to characterize the position relationship between HeLa cells and SMT. The cover glass was placed in the Petri dish, and the cells with a density of about $(4-5) \times 10^4$ cells/mL were seeded into dishes and incubated for 5 h. Then the cells were washed three times with PBS to remove unadhered cells, and DMEM medium and 50 μL of SMT@FITC in PBS suspension were added and incubated in the incubator for 1, 2, 3, and 4 h. The cells were then washed three times with PBS and stained. First, the cells were fixed in 4% paraformaldehyde for 15 min, followed by coculture with 0.5% Triton X-100 solution for 10 min and then with 2% BSA solution for 15 min. Subsequently, phalloidin-TRITC (0.5 μg/mL) solution was added to the culture dish for 30 min to stain the cytoskeleton. Finally, the nuclei were stained by adding 0.03 μg/mL DAPI to the dishes and incubating for 5 min. Wash three times with PBS between each of the above steps. After the staining was completed, a blocked sample was made to facilitate CLSM observation. Two- and three-dimensional characterization of the position of SMT@FITC in relation to HeLa cells using confocal laser scanning microscope (CLSM, Nikon A1). In addition, cells were stained using PI solutions (3 μg/mL) in experiments exploring whether SMT and SMT@Urease could assist in the entry of drugs into cells. The cell seeding plate process and the coculture of cells with artificial transmembrane channels (SMT, SMT@Urease) are as described above. After establishing the artificial transmembrane channels, 1 mL of PI solution was added to the culture dish to coculture with the cells for 20 min, followed by multiple washes with PBS and the preparation of the blocked sample. Finally, the blocked samples were imaged using CLSM. In order to investigate the effect of the SMT structure on the integrity of the cell membrane, we stained the cell membrane with the red membrane dye (DiI). The specific steps are to plant the cells on the confocal dish and wait for 12 h, then add SMT@FITC to coculture with the cells for 4 h, and add DiI to coincubate for 30 min at the ratio of commercial reagent concentration 1:1000; finally, the cells were imaged using CLSM.

Flow Cytometry Analysis. The fluorescence intensity of cell samples was characterized by flow cytometry (Cyto FLEX, Beckman Coulter). After seeding the plates, the cells were incubated continuously until they covered more than 80% of the dish area, and the unadhered cells were removed by washing three times with PBS. In the experiment to explore the effect of SMT on PI transmembrane, 50 μL of PBS solution was added to the control group and 50 μL of SMT solution was added to the experimental group. The samples were cocultured with HeLa cells for 4 h, and then the cells were stained for PI at concentrations of 0, 5, 10, 15, and 20 μg/mL. In the investigation of the effect of SMT@Urease on drug delivery across the membrane, 50 μL of SMT@Urease was added to both control and experimental groups. During the PI staining process, 100 μL of PBS was added to the control group and 100 μL of urea (30 mM) solution was added to the experimental group, and the staining experiments were performed as described above. Then the cells were detached from the culture dish using trypsin and washed by centrifugation to obtain a PBS suspension of the sample. Finally, the PI (red) fluorescence intensity in the target cells was measured by flow cytometry analysis (E_x = 488 nm, E_m = 615 nm).

ASSOCIATED CONTENT

ⓢ Supporting Information

The Supporting Information is available free of charge at https://pubs.acs.org/doi/10.1021/acsnano.3c00291.

SEM, UV–vis spectra, time-lapse snapshots, cell viability results, flow cytometry results, CLSM images, and so on are shown in Figures S1–S14 (PDF)

Video S1: Microjet-1 (SMT-1@Urease) move in 50 mM urea solution (MP4)

Video S2: Microjet-2 (SMT-2@Urease) move in 50 mM urea solution (MP4)

Video S3: Microjet move in a 50 mM urea solution containing tracer particles (MP4)

Video S4: Microjet move in a 50 mM urea solution containing tracer particles (MP4)

Video S5: Microjet move in a 50 mM urea solution containing tracer particles (MP4)

Video S6: Integration of reconstruction processes for 3-D CLSM imaging (MP4)

AUTHOR INFORMATION

Corresponding Author

Xing Ma − *School of Materials Science and Engineering, Harbin Institute of Technology (Shenzhen), Shenzhen, Guangdong 518055, China; Sauvage Laboratory for Smart Materials, Harbin Institute of Technology (Shenzhen), Shenzhen, Guangdong 518055, China;* ⓞ orcid.org/0000-0002-2248-4806; Email: maxing@hit.edu.cn

Authors

Liying Wang − *School of Materials Science and Engineering, Harbin Institute of Technology (Shenzhen), Shenzhen, Guangdong 518055, China; Sauvage Laboratory for Smart Materials, Harbin Institute of Technology (Shenzhen), Shenzhen, Guangdong 518055, China*

Peiting Guo − *School of Materials Science and Engineering, Harbin Institute of Technology (Shenzhen), Shenzhen, Guangdong 518055, China; Sauvage Laboratory for Smart Materials, Harbin Institute of Technology (Shenzhen), Shenzhen, Guangdong 518055, China*

Dongdong Jin − *School of Materials Science and Engineering, Harbin Institute of Technology (Shenzhen), Shenzhen, Guangdong 518055, China; Sauvage Laboratory for Smart Materials, Harbin Institute of Technology (Shenzhen), Shenzhen, Guangdong 518055, China*

Yixin Peng − *School of Materials Science and Engineering, Harbin Institute of Technology (Shenzhen), Shenzhen, Guangdong 518055, China*

Xiang Sun − *State Key Laboratory of Molecular Vaccinology and Molecular Diagnostics, Center for Molecular Imaging and Translational Medicine, School of Public Health, Xiamen University, Xiamen 361005, China*

Yuduo Chen − *School of Materials Science and Engineering, Harbin Institute of Technology (Shenzhen), Shenzhen, Guangdong 518055, China; Sauvage Laboratory for Smart Materials, Harbin Institute of Technology (Shenzhen), Shenzhen, Guangdong 518055, China*

Xiaoxia Liu − *School of Materials Science and Engineering, Harbin Institute of Technology (Shenzhen), Shenzhen, Guangdong 518055, China; Sauvage Laboratory for Smart Materials, Harbin Institute of Technology (Shenzhen), Shenzhen, Guangdong 518055, China*

Wenjun Chen − *School of Materials Science and Engineering, Harbin Institute of Technology (Shenzhen), Shenzhen, Guangdong 518055, China; Sauvage Laboratory for Smart Materials, Harbin Institute of Technology (Shenzhen), Shenzhen, Guangdong 518055, China*

Wei Wang − *School of Materials Science and Engineering, Harbin Institute of Technology (Shenzhen), Shenzhen, Guangdong 518055, China*

Xiaohui Yan − *State Key Laboratory of Molecular Vaccinology and Molecular Diagnostics, Center for Molecular Imaging*

and Translational Medicine, School of Public Health, Xiamen University, Xiamen 361005, China; ⊙ orcid.org/0000-0001-6089-0664

Complete contact information is available at:
https://pubs.acs.org/10.1021/acsnano.3c00291

Author Contributions

REFERENCES

(1) Skou, J. C.; Esmann, M. The Na,K-ATPase. *J. Bioenerg. Biomembr.* 1992, 24, 249−261.

(2) Ghirlanda, G. Changing channels. *Nat. Chem.* 2021, 13, 621−623.

(3) Ghadiri, M. R.; Granja, J. R.; Buehler, L. K. Artificial Transmembrane Ion Channels From Self-Assembling Peptide Nanotubes. *Nature* 1994, 369, 301−304.

(4) Chen, J.; Zhang, B.; Xia, F.; Xie, Y.; Jiang, S.; Su, R.; Lu, Y.; Wu, W. Transmembrane Delivery of Anticancer DrugsThrough Self-Assembly of Cyclic Peptide Nanotubes. *Nanoscale* 2016, 8, 7127−7136.

(5) Geng, J.; Kim, K.; Zhang, J.; Escalada, A.; Tunuguntla, R.; Comolli, L. R.; Allen, F. I.; Shnyrova, A. V.; Cho, K. R.; Munoz, D.; Wang, Y. M.; Grigoropoulos, C. P.; Ajo-Franklin, C. M.; Frolov, V. A.; Noy, A. Stochastic Transport Through Carbon Nanotubes in Lipid Bilayers and Live Cell Membranes. *Nature* 2014, 514, 612−615.

(6) Pan, X.; Xu, D.; Tang, X.; Liu, N.; You, Y.; Wang, X.; Yan, X.; Ma, X.; Chen, X. Endocytosis-Enabled Construction of Silica Nanochannels Crossing Living Cell Membrane for Transmembrane Drug Transport. *Adv. Funct. Mater.* 2020, 30, 2002761.

(7) Silva, R. F.; Araújo, D. R.; Silva, E. R.; Ando, R. A.; Alves, W. A. l-Diphenylalanine Microtubes As a Potential Drug-Delivery System: Characterization, Release Kinetics, and Cytotoxicity. *Langmuir* 2013, 29, 10205−10212.

(8) Song, W.; Joshi, H.; Chowdhury, R.; Najem, J. S.; Shen, Y.-x.; Lang, C.; Henderson, C. B.; Tu, Y.-M.; Farell, M.; Pitz, M. E.; Maranas, C. D.; Cremer, P. S.; Hickey, R. J.; Sarles, S. A.; Hou, J.-l.; Aksimentiev, A.; Kumar, M. Artificial Water Channels Enable Fast and Selective Water Permeation Through Water-Wire Networks. *Nat. Nanotechnol.* 2020, 15, 73−79.

(9) Licsandru, E.; Kocsis, I.; Shen, Y.-x.; Murail, S.; Legrand, Y.-M.; van der Lee, A.; Tsai, D.; Baaden, M.; Kumar, M.; Barboiu, M. Salt-Excluding Artificial Water Channels Exhibiting Enhanced Dipolar Water and Proton Translocation. *J. Am. Chem. Soc.* 2016, 138, 5403−5409.

(10) Kim, K.; Geng, J.; Tunuguntla, R.; Comolli, L. R.; Grigoropoulos, C. P.; Ajo-Franklin, C. M.; Noy, A. Osmotically-Driven Transport in Carbon Nanotube Porins. *Nano Lett.* 2014, 14, 7051−7056.

(11) Joh, N. H.; Wang, T.; Bhate, M. P.; Acharya, R.; Wu, Y.; Grabe, M.; Hong, M.; Grigoryan, G.; DeGrado, W. F. De novo Design of a Transmembrane Zn^{2+}-Transporting Four-Helix Bundle. *Science* 2014, 346, 1520−1524.

(12) Liu, Z.; Winters, M.; Holodniy, M.; Dai, H. siRNA Delivery into Human T Cells and Primary Cells with Carbon-Nanotube Transporters. *Angew. Chem., Int. Ed.* 2007, 46, 2023−2027.

(13) Wang, H.; Pumera, M. Fabrication of Micro/Nanoscale Motors. *Chem. Rev.* 2015, 115, 8704−8735.

(14) Sánchez, S.; Soler, L.; Katuri, J. Chemically Powered Micro- and Nanomotors. *Angew. Chem., Int. Ed.* 2015, 54, 1414−1444.

(15) Wang, B.; Kostarelos, K.; Nelson, B. J.; Zhang, L. Trends in Micro-/Nanorobotics: Materials Development, Actuation, Localization, and System Integration for Biomedical Applications. *Adv. Mater.* 2021, 33, 2002047.

(16) Schmidt, C. K.; Medina-Sánchez, M.; Edmondson, R. J.; Schmidt, O. G. Engineering Microrobots for Targeted Cancer Therapies from a Medical Perspective. *Nat. Commun.* 2020, 11, 5618.

(17) Wang, Y.; Shim, M. S.; Levinson, N. S.; Sung, H.-W.; Xia, Y. Stimuli-Responsive Materials for Controlled Release of Theranostic Agents. *Adv. Funct. Mater.* 2014, 24, 4206−4220.

(18) Esteban-Fernández de Ávila, B.; Angell, C.; Soto, F.; Lopez-Ramirez, M. A.; Báez, D. F.; Xie, S.; Wang, J.; Chen, Y. Acoustically Propelled Nanomotors for Intracellular siRNA Delivery. *ACS Nano* 2016, 10, 4997−5005.

(19) Xi, W.; Solovev, A. A.; Ananth, A. N.; Gracias, D. H.; Sanchez, S.; Schmidt, O. G. Rolled-up Magnetic Microdrillers: Towards Remotely Controlled Minimally Invasive Surgery. *Nanoscale* 2013, 5, 1294−1297.

(20) Sanchez, S.; Solovev, A. A.; Schulze, S.; Schmidt, O. G. Controlled Manipulation of Multiple Cells Using Catalytic Microbots. *Chem. Commun.* 2011, 47, 698−700.

(21) Patino, T.; Porchetta, A.; Jannasch, A.; Lladó, A.; Stumpp, T.; Schäffer, E.; Ricci, F.; Sánchez, S. Self-Sensing Enzyme-Powered Micromotors Equipped with pH-Responsive DNA Nanoswitches. *Nano Lett.* 2019, 19, 3440−3447.

(22) Xuan, M.; Shao, J.; Gao, C.; Wang, W.; Dai, L.; He, Q. Self-Propelled Nanomotors for Thermomechanically Percolating Cell Membranes. *Angew. Chem., Int. Ed.* 2018, 57, 12463−12467.

(23) Esteban-Fernandez de Avila, B.; Ramirez-Herrera, D. E.; Campuzano, S.; Angsantikul, P.; Zhang, L.; Wang, J. Nanomotor-Enabled pH-Responsive Intracellular Delivery of Caspase-3: Toward Rapid Cell Apoptosis. *ACS Nano* 2017, 11, 5367−5374.

(24) Zhang, F.; Zhuang, J.; Esteban Fernandez de Avila, B.; Tang, S.; Zhang, Q.; Fang, R. H.; Zhang, L.; Wang, J. A Nanomotor-Based Active Delivery System for Intracellular Oxygen Transport. *ACS Nano* 2019, 13, 11996−12005.

(25) Wang, W.; Wu, Z.; Lin, X.; Si, T.; He, Q. Gold-Nanoshell-Functionalized Polymer Nanoswimmer for Photomechanical Poration of Single-Cell Membrane. *J. Am. Chem. Soc.* 2019, 141, 6601−6608.

(26) Srivastava, S. K.; Medina-Sánchez, M.; Koch, B.; Schmidt, O. G. Medibots: Dual-Action Biogenic Microdaggers for Single-Cell Surgery and Drug Release. *Adv. Mater.* 2016, 28, 832−837.

(27) Sun, M.; Liu, Q.; Fan, X.; Wang, Y.; Chen, W.; Tian, C.; Sun, L.; Xie, H. Autonomous Biohybrid Urchin-Like Microperforator for Intracellular Payload Delivery. *Small* 2020, 16, 1906701.

(28) Vilela, D.; Hortelao, A. C.; Balderas-Xicohténcatl, R.; Hirscher, M.; Hahn, K.; Ma, X.; Sánchez, S. Facile Fabrication of Mesoporous Silica Micro-jets with Multi-Functionalities. *Nanoscale* 2017, 9, 13990−13997.

(29) Xu, D.; Zhou, C.; Zhan, C.; Wang, Y.; You, Y.; Pan, X.; Jiao, J.; Zhang, R.; Dong, Z.; Wang, W.; Ma, X. Enzymatic Micromotors as a Mobile Photosensitizer Platform for Highly Efficient On-Chip Targeted Antibacteria Photodynamic Therapy. *Adv. Funct. Mater.* 2019, 29, 1807727.

(30) Jin, X.; Wang, Q.; Sun, J.; Panezai, H.; Bai, S.; Wu, X. Dual (pH- and temperature-) Stimuli Responsive Nanocarrier with

Bimodal Mesoporous Silica Nanoparticles Core and Copolymer Shell for Controlled Ibuprofen-Releasing: Fractal Feature and Diffusion Mechanism. *Microporous Mesoporous Mater.* **2017**, *254*, 77−85.

(31) Savinkina, E. V.; Golubev, D. V.; Grigoriev, M. S. Ionic Acetamide Coordination in Its Complexes with Rare-Earth Iodides. *J. Coord. Chem.* **2011**, *64*, 3758−3766.

(32) Arqué, X.; Romero-Rivera, A.; Feixas, F.; Patiño, T.; Osuna, S.; Sánchez, S. Intrinsic Enzymatic Properties Modulate the Self-Propulsion of Micromotors. *Nat. Commun.* **2019**, *10*, 2826.

(33) Ma, X.; Hortelao, A. C.; Miguel-Lopez, A.; Sanchez, S. Bubble-Free Propulsion of Ultrasmall Tubular Nanojets Powered by Biocatalytic Reactions. *J. Am. Chem. Soc.* **2016**, *138*, 13782−13785.

(34) Ortiz-Rivera, I.; Shum, H.; Agrawal, A.; Sen, A.; Balazs, A. C. Convective flow reversal in self-powered enzyme micropumps. *Proc. Natl. Acad. Sci. U. S. A.* **2016**, *113*, 2585−2590.

(35) Gao, W.; Dong, R.; Thamphiwatana, S.; Li, J.; Gao, W.; Zhang, L.; Wang, J. Artificial Micromotors in the Mouse's Stomach: A Step toward in Vivo Use of Synthetic Motors. *ACS Nano* **2015**, *9*, 117−123.

(36) Solovev, A. A.; Sanchez, S.; Pumera, M.; Mei, Y. F.; Schmidt, O. G. Magnetic Control of Tubular Catalytic Microbots for the Transport, Assembly, and Delivery of Micro-objects. *Adv. Funct. Mater.* **2010**, *20*, 2430−2435.

(37) Sanchez, S.; Solovev, A. A.; Mei, Y.; Schmidt, O. G. Dynamics of Biocatalytic Microengines Mediated by Variable Friction Control. *J. Am. Chem. Soc.* **2010**, *132*, 13144−13145.

(38) Sengupta, S.; Patra, D.; Ortiz-Rivera, I.; Agrawal, A.; Shklyaev, S.; Dey, K. K.; Córdova-Figueroa, U.; Mallouk, T. E.; Sen, A. Self-Powered Enzyme Micropumps. *Nat. Chem.* **2014**, *6*, 415−422.

(39) Das, S.; Shklyaev, O. E.; Altemose, A.; Shum, H.; Ortiz-Rivera, I.; Valdez, L.; Mallouk, T. E.; Balazs, A. C.; Sen, A. Harnessing Catalytic pumps for Directional Delivery of Microparticles in Microchambers. *Nat. Commun.* **2017**, *8*, 14384.

(40) Valdez, L.; Shum, H.; Ortiz-Rivera, I.; Balazs, A. C.; Sen, A. Solutal and Thermal Buoyancy Effects in Self-Powered Phosphatase Micropumps. *Soft Matter* **2017**, *13*, 2800−2807.

(41) Maiti, S.; Shklyaev, O. E.; Balazs, A. C.; Sen, A. Self-Organization of Fluids in a Multienzymatic Pump System. *Langmuir* **2019**, *35*, 3724−3732.

(42) Shklyaev, O. E.; Shum, H.; Sen, A.; Balazs, A. C. Harnessing Surface-Bound Enzymatic Reactions to Organize Microcapsules in Solution. *Sci. Adv.* **2016**, *2*, e1501835.

(43) Ortiz-Rivera, I.; Courtney, T. M.; Sen, A. Enzyme Micropump-Based Inhibitor Assays. *Adv. Funct. Mater.* **2016**, *26*, 2135−2142.

(44) Jun, I.-K.; Hess, H. A Biomimetic, Self-Pumping Membrane. *Adv. Mater.* **2010**, *22*, 4823−4825.

(45) Sengupta, S.; Spiering, M. M.; Dey, K. K.; Duan, W.; Patra, D.; Butler, P. J.; Astumian, R. D.; Benkovic, S. J.; Sen, A. DNA Polymerase as a Molecular Motor and Pump. *ACS Nano* **2014**, *8*, 2410−2418.

(46) Chiang, T.-Y.; Velegol, D. Localized Electroosmosis (LEO) Induced by Spherical Colloidal Motors. *Langmuir* **2014**, *30*, 2600−2607.

(47) Zhou, C.; Zhang, H. P.; Tang, J.; Wang, W. Photochemically Powered AgCl Janus Micromotors as a Model System to Understand Ionic Self-Diffusiophoresis. *Langmuir* **2018**, *34*, 3289−3295.